



# Effect of Irradiation on Ni-Inconel/Incoloy Heterostructures in Multimetallic Layered Composites



Shiddartha Paul<sup>a</sup>, Daniel Schwen<sup>b</sup>, Michael P. Short<sup>c</sup>, Kasra Momeni<sup>a,\*</sup>

<sup>a</sup> Department of Mechanical Engineering, University of Alabama, Tuscaloosa, AL 35487, United States

<sup>b</sup> Department of Computational Mechanics and Materials, Idaho National Laboratory, Idaho Falls, ID 83402, United States

<sup>c</sup> Department of Nuclear Science & Engineering, Massachusetts Institute of Technology, Cambridge, MA 02139, United States

## ARTICLE INFO

### Article history:

Received 29 August 2020

Revised 26 December 2020

Accepted 31 December 2020

Available online 21 January 2021

### Keywords:

Radiation resistant materials  
Multi-metallic layered composite (MMLC)  
Molecular dynamics  
Generation IV nuclear reactors  
High entropy alloys

## ABSTRACT

We use molecular dynamics (MD) to study radiation-induced mixing through multi-metallic layered composites' interfaces for nuclear reactor applications. Here, we consider the Incoloy-Ni and the Inconel-Ni system with four different compositions of Inconel. We investigate the irradiated structure of these composites at different temperatures by performing successive 10 keV collision cascades simulations up to the radiation dose of 0.5 displacements per atom (dpa). We reveal a linear relationship between the interface thickness of the heterostructure with the radiation dose and the higher tendency of Cr for penetration in Ni. The lower migration barrier of Cr assists the formation of vacancies and interstitials. Our results indicate that the Incoloy 800H (Ni<sub>32</sub>Cr<sub>21</sub>Fe<sub>47</sub>) has a high radiation resistance among all the considered compositions.

Published by Elsevier B.V.

## 1. Introduction

The critical challenge in Generation IV nuclear reactors' design is developing low-cost materials that can maintain their integrity under harsh reactor environments beyond 60 years [1]. For example, developing new radiation-resistant structural materials for high temperatures and corrosive environments is one of the crucial obstacles for building these reactors [2]. Following a classic approach of making new do-it-all alloys is very time consuming and requires extensive testing. Because an ASME code case does not exist for newly developed materials, and it will need at least seven years of testing, that itself will be a barrier to their fast deployment.

Multimetallic Layered Composites (MMLC) provide a unique solution to this complex problem by decoupling interactions between different alloys through forming a functionally graded material. It allows the use of existing ASME code cases for each layer to be applied to the entire structural design. MMLCs have shown potential for developing accident tolerant fuel cladding of light water reactors [3], in the lead- and lead-bismuth-cooled nuclear reactors [4], and fluoride-salt-cooled high-temperature reactors [5]. Here, we investigate the stability and formation of interfacial phases under irradiations for two MMLC systems with potential application

in the next-generation nuclear reactors: (i) Ni-Fe-Cr/Ni, and (ii) Inconel/Ni. The Ni-Fe-Cr alloys have an excellent oxidation resistance for fuel cladding [6] and an enhanced defect recombination rate compared to the bulk Ni or the Ni-Fe system desired for cladding materials [7]. Inconel [8] is a candidate material for cladding due to its high mechanical strength [9,10], swelling [11–13] resistance, and excellent oxidation-corrosion resistance [14].

Understanding the radiation-induced damage is vital for gaining insight into the microstructural evolution of materials for nuclear applications and predicting their structural integrity over their lifetime. Radiation flux has a multifaceted effect on materials, such as an increase in the concentration of point defects and variation of composition in the vicinity of sinks, which is known as radiation-induced segregation [15]. This effect in Fe-Cr alloys causes Cr enrichment or depletion, leading to corrosion sensitivity or embrittlement [16]. One of the critical issues adversely affecting the structural integrity of the irradiated materials is the radiation-enhanced diffusion due to the formation of vacancies, interstitials, and point defects. These defects deteriorate the mechanical and thermal properties [17,18] and affect dimensions of cladding materials through embrittlement, radiation-induced creep, and swelling [19–21]. These effects can hamper the reactor's regular and safe operation by creating malfunctions like cooling disruption and crack formation in different structural parts of a reactor, leading to catastrophic failures and a severe accident.

Experimental studies have been performed to understand the change in material properties due to irradiation, such as

\* Corresponding author.

E-mail address: [kmomeni@ua.edu](mailto:kmomeni@ua.edu) (K. Momeni).

microstructure evolution, cracking, and embrittlement [22]. However, these tests are challenging due to the high costs of sample preparation, controlled radiation, and characterization of irradiated samples. Computer simulations provide an alternative tool to study irradiation's effect on the structural integrity and variation of material properties during their life. These simulations provide insight into alloys' behavior under irradiation across different length and temporal scales [23,24].

In this study, we used the molecular dynamics technique to investigate radiation's effect on the interfaces' structural integrity in Inconel/Ni and Incoloy 800H/Ni MMLCs. We performed a systematic study of alloy composition on the radiation-induced defect formation and interface properties, such as width, in these materials. The presented results provide a fundamental understanding of the role of alloys' chemistry on the structural integrity of MMLCs under extreme radiations and temperatures for use as a cladding material.

## 2. Computational methodology

We have considered four compositions of Inconel and one Incoloy 800H for an  $80 \times 40 \times 40$  face-centered cubic (FCC) lattice structures of Nickel (Ni) with 512000 atoms. This system size ensures that the collision cascades initiated by 10 keV PKAs do not interact with the periodic images while modeling the many cascades that are yet computationally tractable. The four sample Inconel structures are  $\text{Ni}_{51}\text{Cr}_{30}\text{Fe}_{19}$ ,  $\text{Ni}_{56}\text{Cr}_{23}\text{Fe}_{21}$ ,  $\text{Ni}_{60}\text{Cr}_{21}\text{Fe}_{19}$ , and  $\text{Ni}_{51}\text{Cr}_{25}\text{Fe}_{24}$ , and the one Incoloy 800H structure is  $\text{Ni}_{32}\text{Cr}_{21}\text{Fe}_{47}$ . The lattice constant of Inconel and Ni calculated by the EAM-1 potential is 3.62 Å and 3.52 Å, respectively. The experimentally measured lattice constants of Inconel and Ni are 3.60 Å [25] and 3.58 Å [26], respectively. Here, we used the experimentally measured lattice constant of Inconel, 3.60 Å [25], to build our model material. We then replaced the Ni atoms on half of the sample with Fe and Cr atoms according to their molar percentage, turning half of the sample into the associated alloy structure with  $40 \times 40 \times 40$  units. We have applied periodic boundary conditions in all directions. We performed our simulations using the Large-scale Atomic/Molecular Massively Parallel Simulator (LAMMPS) open-source code [27].

There are three Embedded Atom Model (EAM) potentials for the Ni-Cr-Fe, which we designate with EAM-1 [28], EAM-2 [29], and EAM-3 [30]. We have chosen EAM-1 potential since it can capture Fe-Cr-Ni metallic alloys' behavior at different conditions (see the Supplementary Material). Particularly, the stacking fault energy calculated by the EAM-1 potential has a good agreement with the experimental values for a wide range of alloying element compositions [28]. To investigate the independence of our results from the chosen potential, we have compared different material properties calculated by these potentials. The elastic constants and vacancy formation energy calculated by EAM-1 are in good agreement with the values calculated with EAM-2 and EAM-3 potentials and experimentally measured values (see Tables 1 and 2). We have also performed cascade simulations for each potential to ensure that our results are not affected by the forcefield artifacts. We have presented a comparison of the radiation enhanced diffusion (RED) coefficient to measure radiation damage for different potentials in Figure 1. Our results indicate that the average value of the RED coefficient calculated by EAM-1 is close to the averages obtained by EAM-2 and EAM-3. The EAM-2 potential has already been used to model Fe-Cr-Ni alloys' radiation damage in different studies [29,31–33].

We modified the EAM interatomic potential by adding the Ziegler-Biersack-Littmark (ZBL) [34,35] potential (see Supplementary Materials) to describe the short-range and high energy collisions during the high energy cascade simulations. The expression

**Table 1**

Vacancy formation energy,  $E_{fv}$ , of Cr, Fe, and Ni for different EAM potentials. The results are independent of the chosen potential and in good agreement with experiments.

Elements	EAM potential	$E_{fv}$ (eV)
Cr	EAM-1 [28]	2.09
	EAM-2 [29]	2.25
	EAM-3 [30]	1.98
	Experiment [36]	2.56
Fe	EAM-1 [28]	2.13
	EAM-2 [29]	1.94
	EAM-3 [30]	1.58
	Experiment [37]	2.17
Ni	EAM-1 [28]	1.79
	EAM-2 [29]	1.47
	EAM-3 [30]	1.50
	Experiment [38]	1.68

**Table 2**

Comparing the mechanical properties of Inconel ( $\text{Ni}_{51}\text{Cr}_{24}\text{Fe}_{25}$ ) for the EAM and ZBL modified EAM potentials. The addition of the ZBL potential term does not alter these properties.

Case	$G$ (ksi $\times 10^3$ )	$E$ (ksi $\times 10^3$ )	$\nu$
EAM-1	20.61	47.32	0.18
EAM-2	27.55	62.21	0.13
EAM-3	18.20	43.66	0.20
ZBL modified EAM-1	20.61	47.32	0.18
Experiment [47]	12.50	31.30	0.25

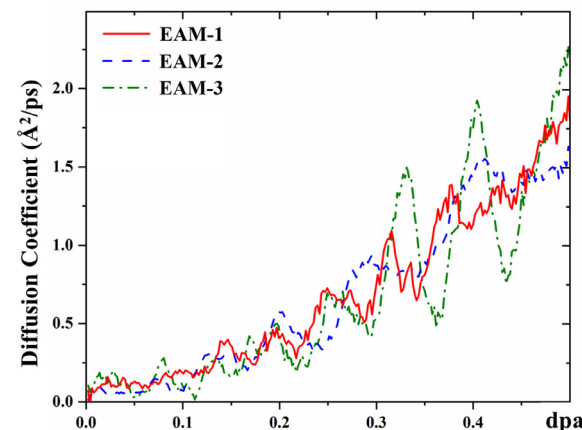


**Figure 1.** Radiation enhanced diffusion coefficient of Inconel ( $\text{Ni}_{51}\text{Cr}_{24}\text{Fe}_{25}$ )/Ni MMLC. The calculated diffusion coefficient at 1000K shows similar average values for the different interatomic potentials, indicating the results' potential-independence.

for the total energy is

$$E_{\text{Tot}} = E_{\text{EAM}}H(r_{ij}) + E_{\text{ZBL}}(1 - H(r_{ij})), \quad (1)$$

where  $H(r_{ij})$  is the Heaviside function to ensure the smooth transition between EAM and ZBL potentials.

The ZBL-modified EAM potential has a steeper curve close to the nucleus compared to the EAM potential. The first nearest neighbor atom in an FCC crystal is at  $0.707a$ , where  $a$  is the lattice constant, and thus, the inner and outer radius of ZBL potential should be less than this distance. For Nickel, this distance is 2.49 Å. We assumed the same cutoff radius as the initial pristine EAM potential for associated pairwise interactors. We determined the inner and outer radii of the ZBL modified EAM potential following a trial and error process, where the difference between the ZBL-modified and pristine potentials was minimized. We choose the inner and outer radii values of 0.9 and 1.25 Å, respectively (Figure 2(a)). Figure 2(a) shows the variation of the EAM and ZBL-

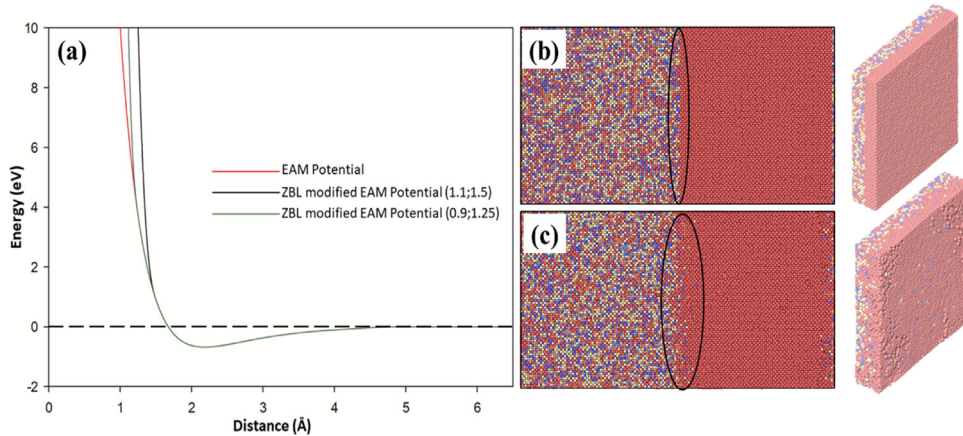


**Figure 2.** Interatomic potentials utilized and the simulated structures. (a) Interatomic potential plots for the pure EAM and ZBL modified EAM potentials; (b) initial and (c) the final 800H structure after 300 PKAs introduced (final stage) to implement the irradiation, the corresponding zoomed slices of the interfacial phases are shown on the right.

modified EAM (for two different inner and outer radii pairs of values) interatomic potentials as a function of the separation distance between two atoms. We compared the elastic modulus,  $E$ , shear modulus,  $G$ , and Poisson's ratio,  $\nu$ , of bulk Inconel samples for both pristine and ZBL-modified potentials, Table 2, which indicates that adding the ZBL potential term does not change these mechanical properties. The difference between the predicted and experimentally measured values could be due to the EAM potentials' limitations for modeling ternary alloys. Furthermore, we compared our calculated mechanical properties with the ones reported for the other potentials. However, we could not find any noticeable discrepancy between these calculated properties, Table 2.

The MD technique has been used to investigate the effect of irradiation damage in materials at various temperatures, such as irradiation of  $\text{UO}_2$  between 700–1800K with Uranium atoms with a PKA of 10 keV [39]. The radiation damage was determined by considering vacancies and formed defects using Seitz's theory [40] of moving atoms.

Both NVT [41] and NPT [42] relaxations have been used to study the effect of irradiation in materials. Here, we carried out the MD simulations by initially relaxing the structure at 1000K – the typical operating temperature of fluoride-salt high-temperature reactors – for 50ps with a time step of 1fs in the NVT ensemble. The use of NVT relaxation leads to small strains of 0.005 and 0.02 on the Inconel and Ni sides with respect to the EAM-1 lattice parameters, respectively. We could not realize major differences between the stresses calculated for our system when the NPT ensemble was used during the relaxation phase. Then for the cascade simulation, we randomly select a primary knock-on atom (PKA) and set its velocity to the equivalent 10 keV cascade energy. The dose rate in MD simulation is orders of magnitude higher than the experimental doses [43], which is due to the inherent limitation of this method for modeling events in the scales of a few nanoseconds that subsequently yield in short simulation time between the collision cascades. However, implanted ion distribution (PKA in our case) at relatively lower ion energy in the order of 10keV could successfully reproduce the experimentally observed irradiation damage due to irradiations at MeV energies [32,44–46]. We did not differentiate the atoms based on their radiation transparency because it is relatively the same for the elements considered in this study. The velocity has been distributed in different directions, where the absolute velocity value corresponding to 10 keV energy is set to be maximum in the direction normal to the Inconel–Ni heterostructure interface, i.e.,  $\nu = (0.99, 0.135, 0.042)|\nu|$ . The cascade simulation carried out for 20ps in NVE ensemble

with a variable time step algorithm to maintain the numerical efficiency.

Figure 2(b)–(c) shows that the interface structure during the initial and final state of cascade simulation and mixing are shown, respectively. These simulations indicate that the Inconel–Ni interface transforms from a sharp bilayer heterostructure interfaces, Figure 2(b), to a system that contains interstitials and vacancies, Figure 2(c), by increasing the radiation dose. As the radiation dose increases, the Ni, Cr, and Fe atoms of the Inconel gradually diffuse in pure Ni due to the ballistic intermixing and form various vacancies and impurities.

When the PKA initiates, it dissipates the kinetic energy within a short free path and in the first 0.9–1.5ps of the simulation. The energy range that we are studying (~10keV) correlates to the very short-lived thermalized regime during displacement cascade, which can be defined as a thermal spike (TS) region [48,49]. TS region forms when the maximum cascade energy dissipated to the neighboring atoms within ~1ps of the PKA initiation. The TS quenched back to 1000K at the end of the collision cascade, after 0.8–1ps. Afterward, we have annealed the structure under the NVT ensemble for 5ps. We have calculated the dpa per PKA atom using the Stopping and Range of Ions in Materials (SRIM) code [34], where we came to 0.002 dpa/PKA. We repeat the cascade simulation to model the material response at higher radiation doses. We performed a total of 250 recoil simulations to achieve damage up to 0.5dpa. In this study, we have assumed frictionless collision cascades and neglected the electronic stopping [24,50]. This assumption leads to an overestimation of the damage and an inherent safety factor. Electronic stopping can be modeled by introducing a friction term in the equation of motion of atoms [51–53].

The Norgett–Robinson–Torrens (NRT) equation for determining the number of displacements per atom for a PKA is  $dpa = 0.4T_{dam}E_{PKA}/E_d$ . Here,  $T_{dam}$  is the damage energy, and  $E_d$  is the threshold displacement of energy.  $T_{dam}$  can be calculated by the following equation  $T_{dam} = E_i^B + E_T^B + E_i^P + E_T^P$ . Here  $E_i^B$  is the beam energy lost to lattice binding energy;  $E_T^B$  is the energy needed for creating one vacancy or the target atom energy lost to lattice binding energy and equals to lattice binding energy  $E_B$  multiplied by the number of vacancies created by target atoms  $\nu_T$ . Here, we considered  $E_B = 3.32$  eV of Ni, and  $\nu_T = 1/512000$  since we have 512,000 atoms in our simulation cell. Furthermore,  $E_i^P$  is the beam energy lost to phonons and  $E_T^P$  is the target atom energy lost to phonons. In our case, the calculated dpa using NRT model without considering the phononic phenomenon for the 250 PKAs of 10KeV, using  $E_d = 23$ eV for Ni [54] and  $T_{dam} = 3.32$  eV from SRIM simula-

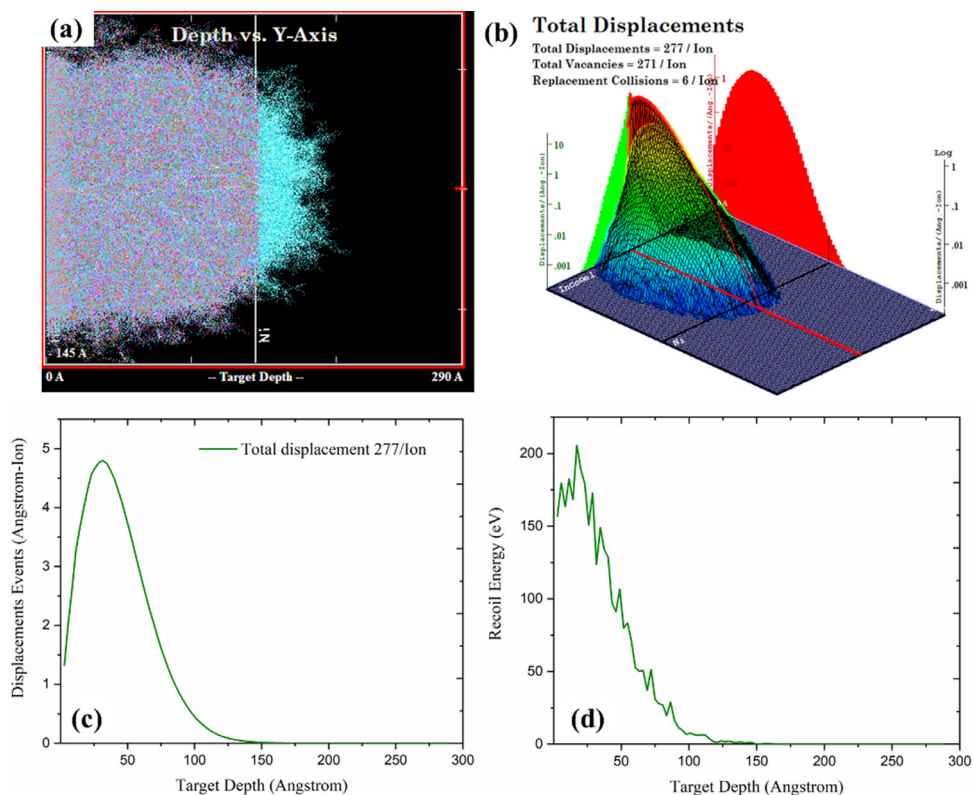


**Figure 3.** SRIM set up for Ni-based MMLC radiation simulation. (a) Ni-Inconel ( $\text{Ni}_{51}\text{Cr}_{24}\text{Fe}_{25}$ ) structure details with the 10 keV energy PKA; (b) Radiation displacement log-log plot along the three-dimensional surfaces of the Ni-Inconel heterostructure; (c) Number of displacements per angstrom of thickness for each incident ion; (d) Deposition energy as a function of the target depth along with the interface.

tions is

$$dpa = 0.4 \times \left( 3.32 \text{ eV} \times \frac{1}{512000} \right) \\ \times 250 \times 10000(\text{eV/PKA})/23 \text{ eV} = 0.2819,$$

which is 44% smaller than the value calculated by SRIM. One of the sources of discrepancy between NRT calculated values and SRIM simulations is the complexity of our system, where we considered an MMLC of alloys. For example, for an MMLC system of simple metal elements, there was a 20% discrepancy between the predicted SRIM calculations and rough NRT estimates [55]. Furthermore, here the PKAs are randomly initiated from the Inconel side with  $0^\circ$  knock on direction, not from the whole structure.

### 3. Results and Discussion

We have simulated the Ni-Ni alloy heterostructure for five different compositions, i.e., four Inconel ( $\text{Ni}_{51}\text{Cr}_{30}\text{Fe}_{19}$ ,  $\text{Ni}_{56}\text{Cr}_{23}\text{Fe}_{21}$ ,  $\text{Ni}_{60}\text{Cr}_{21}\text{Fe}_{19}$ , and  $\text{Ni}_{51}\text{Cr}_{25}\text{Fe}_{24}$ ), and one Incoloy 800H ( $\text{Ni}_{32}\text{Cr}_{21}\text{Fe}_{47}$ ). Cascade formation was identified by introducing the PKAs. Atoms from the alloy mix into the pure Ni by increasing the radiation dose. As radiation increases, the sharp interface transforms into a diffuse interface with vacancies and interstitials. In this study, we have analyzed the effect of alloying compositions of Ni-Cr-Fe composite (Inconel and Incoloy 800H) on the radiation-induced mixing in the Ni-Inconel/Incoloy MMLCs.

#### 3.1. Calculation of dpa

Kinchin et al. [56] have developed a mathematical model to calculate dpa by considering the kinetic energy above a threshold displacement energy. We have used the SRIM [34] code to calculate dpa, where we used the same structures, composition, and recoil

cascade energy as we used for the MD simulations, i.e., 10 keV. We set the radiation depth up to 288 Å (= 80 unit cells  $\times$  3.6 Å unit cell length). Figure 3(a) shows the ion incident on the target Ni-Inconel ( $\text{Ni}_{51}\text{Cr}_{24}\text{Fe}_{25}$ ) layer, which led to mixing the Inconel atoms through the interface. We used 99999 ion incidents to have a statistically representative calculation. Figure 3(b) shows the log-log plot of displacement and its distribution over the layers, where part of the displacement field crossed the interface, leading to the mixing of Inconel and Ni atoms. Figure 3(b) also shows the number of displacements and vacancies. We calculated the number of displacements per ion-angstrom to be 4.6, Figure 3(c), which we then used to calculate the dpa (see Supplemental Information). Figure 3(d) shows the nuclear-deposited energy equivalent to the radiation as a function of the target's depth.

The fluence area is the Ni-Inconel interface cross-section, and we assumed the radiation source to be on the Inconel side. We have calculated the atomic volume using the weighted average of the atomic radius of Ni, Cr, and Fe because the PKAs are randomly selected.

#### 3.2. Effect of Alloy Composition

We studied the effect of alloy composition on the intermixing of different alloying elements under irradiation and the interface's stability and formation of vacancies and interstitials. Comparing the Cr and Fe atoms' profile at the interface, Figure 4, reveals the higher intermixing of Cr compared to Fe. This result is consistent with previous reports on the lower migration barrier of Cr in comparison with Ni and Fe [57]. We have further calculated the migration energy barrier of Ni, Fe, and Cr through the Ni lattice using the EAM-1 potential [28], which is comparable with other reported literature values calculated using EAM-2 potential and the

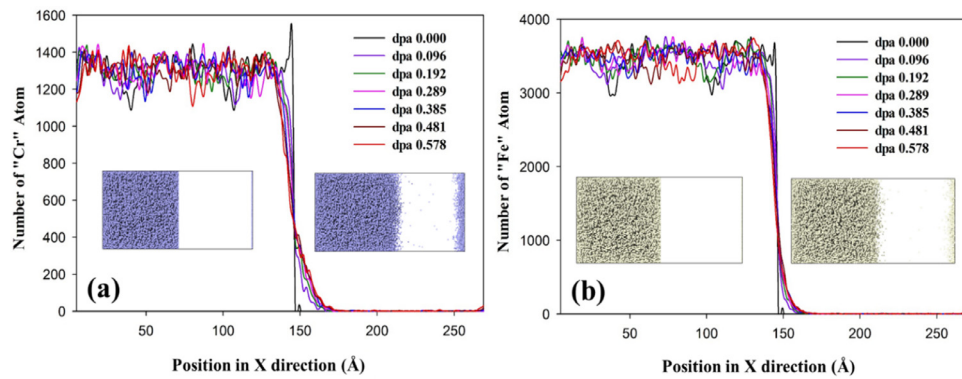


**Figure 4.** Intermixing of alloying elements under irradiation. (a,b) Mixing profiles of Cr and Fe atoms, respectively, at different positions in the x-direction for 800H. The Cr and Fe mixing profiles for other alloying compositions have been presented in [Appendix B](#).

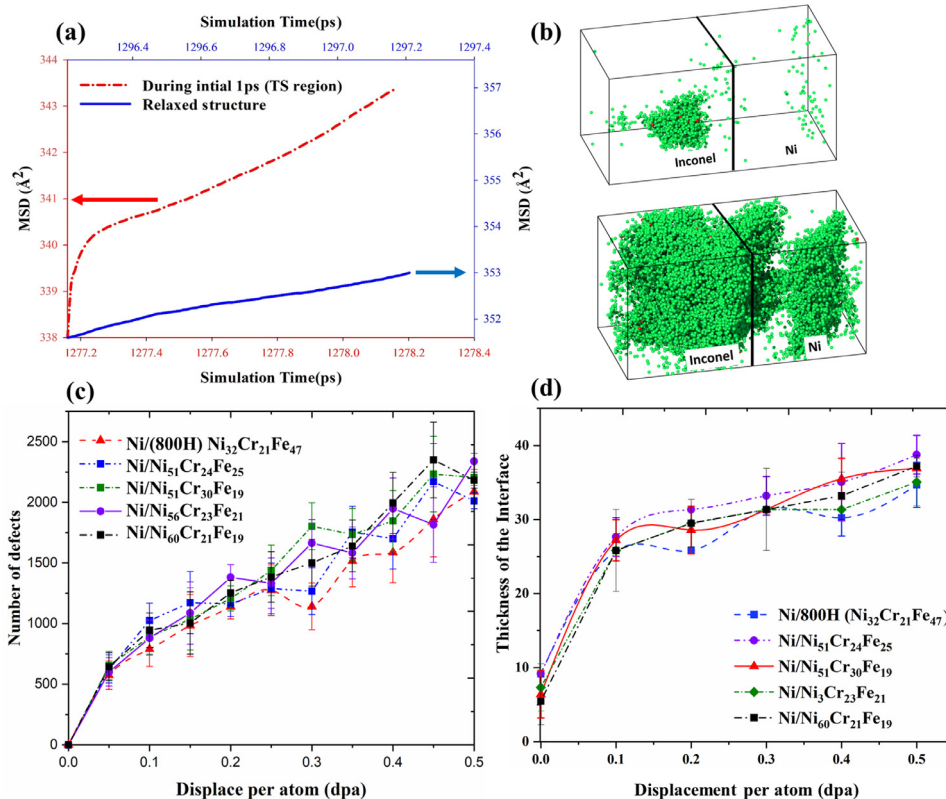


**Figure 5.** Effect of radiation on the formation of defects and intermixing of different elements. (a) MSD during the initial and final step of the 50<sup>th</sup> cascade event; (b) accumulated defects for  $\text{Ni}_{51}\text{Cr}_{30}\text{Fe}_{19}$  in the simulation box during the 1<sup>st</sup> PKA (top) and after the 300<sup>th</sup> PKAs (bottom); (c) Accumulation of defects, both Frenkel pairs defects, as a function of dpa; and (d) Interface thickness of different Inconel compositions with pure Ni as a function radiation damage in dpa.

**Table 3**  
Migration energy (eV) of different atoms in FCC lattice of Ni.

Element	Migration barrier using MD Our values (EAM-1)	Ref. [31] (EAM-2)	Migration barrier using DFT [31]
Ni	1.09	1.08	1.08
Fe	1.06	1.02	0.95
Cr	0.64	0.71	0.75

DFT method [29,31]; see [Table 3](#). We can see that Cr has a lower migration barrier, resulting in a faster diffusion rate than the other alloying elements.

To understand the effect of radiation on the overall mixing of elements, we calculated the mean squared displacement (MSD) of all atoms as a function of time during a cascade event, [Figure 5\(a\)](#).

This method is the standard method for measuring the mixing in MD simulations [58,59]. The MSD can also be connected to the Mixing Parameter, a measure for determining the Radiation-Induced Mixing, by dividing MSD with the model's atomic density and deposited nuclear energy [60]. A more accurate way of calculating the Mixing Parameter has been introduced following the Boltzman-Matano approach [42]. The current MSD calculations are yet sufficient to understand the role of alloy chemistry on the radiation-induced mixing and compare the performance of different compositions.

We considered two time periods, i.e., the first and the last 1ps of the cascade event, for a radiation dose of 0.1dpa (50<sup>th</sup> PKA event) that led to a diffuse interface width  $\sim 20\text{\AA}$ . Our results revealed a rapid increase in the MSD of all atoms during the first 1ps of the cascade, i.e., the TS region. In contrast, at the ending 1ps pe-

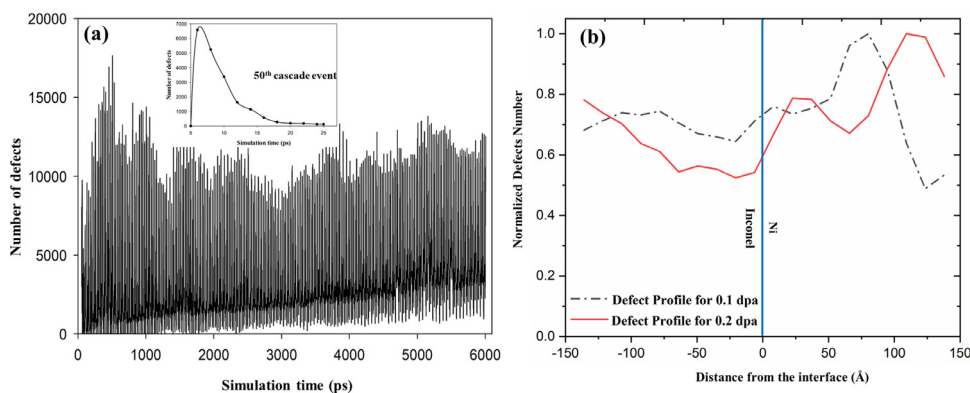


**Figure 6.** Formation and annihilation of defects during irradiation. (a) The defect formation throughout simulation; The inset figure shows the defect formation and annihilation during the 50th cascade event. A linear relation between the number of defects (vacancies and interstitials) and the number of cascade events is revealed. (b) defect formation profile at different dpa.

riod of the cascade event, the rate of change of MSD as a function of radiation dose becomes constant. Since the diffusion coefficient is proportional to the MSD vs. time curve slope, Figure 5(a) indicates the maximum mixing during the TS region.

Figure 5(b) shows the formation of the defects (vacancies and interstitials) as cascade events go on. The formation of a cluster of interstitials is revealed in the irradiated Inconel during the initial irradiation stage. By continuing the irradiation process, defect clusters will evenly distribute in both Inconel and Ni. This distribution pattern could be due to the high temperature at which we performed our simulations, i.e., 1000K, as the intermixing of defects is a strong function of temperature [61]. Small vacancy clusters form in Ni have higher mobility than the ones form in NiFe alloys [21]. The lower defect mobility in NiFe alloys is due to the chemical disorder that arises from the composition complexity. A higher point defect migration tendency in Ni helps to aggravate cluster formation during successive cascades [32]. We also studied the distribution of defects, where we could not detect any statistically meaningful effect of the (100) interface.

The Wigner-Seitz cell [62] method has been used to identify the defects, where the damaged sample has been compared to the reference (initial) structure. Figure 5(c) indicates that the number of vacancies and interstitials increases with the radiation dose. It also revealed that the total number of vacancies and interstitials in the 800H ( $\text{Ni}_{32}\text{Cr}_{21}\text{Fe}_{47}$ ) alloy is the least among the considered compositions, and the alloys with lower iron content are more prone to the formation of defects under irradiation. Furthermore, in the case of Inconel  $\text{Ni}_{51}\text{Cr}_{30}\text{Fe}_{19}$ , the slope of radiation-induced defects increases by increasing the dpa. We also revealed that Cr promotes defect accumulation by intermixing through defect assisted diffusion. Our results are consistent with previous reports showing that Cr promotes Ni diffusion and defect accumulation in irradiated binary and ternary Ni-Cr-Fe alloys [31].

We also revealed that the interface's thickness, which characterizes the intermixing, increases by increasing the radiation dose, Figure 5(d). We found that the 800H and  $\text{Ni}_{60}\text{Cr}_{21}\text{Fe}_{19}$  have the lowest and highest thickness at radiation doses below 0.5 dpa, respectively. However, the thickness for  $\text{Ni}_{51}\text{Cr}_{30}\text{Fe}_{19}$  dominates when the radiation dose increases further due to the Cr induced mixing. Our results indicate that the variation in the alloy composition impacts the radiation-induced damage. Particularly, we revealed that the concentration of defects is minimum in Incoloy 800H, which has the highest iron concentration. Thus, we conclude that iron-rich alloys have a higher radiation resistance, consistent with previous experimental reports [63].

We further studied the effect of radiation dose on the formation of defects, where we revealed their linear correlation, Figure 6.

Vacancies and interstitials annihilate beyond the TS region during each cascade event's quenching or cooling phase; see the inset image in Figure 6(a). However, the increase in the number of irradiation-induced defects as a function of time indicates that they will not recover completely. Interfaces and grain boundaries may act as defect sinks, increasing radiation damage tolerance depending on the misorientation angle or interface plane [64,65]. We studied the distribution of defects across the MMLC, Figure 6 (b), revealing no definite defect segregation trend near the Inconel/Ni interface. The zero misorientation angle could explain the negligible effect of the (100) interface.

The diffusion coefficient is directly related to the mixing parameter ( $MP$ ), which describes the radiation-induced mixing as  $MP = \frac{Dt}{\varphi F_D}$ , where  $D$  is the diffusion coefficient,  $t$  is the irradiation time,  $\varphi$  is the ion fluence, and  $F_D$  is the deposited nuclear energy per unit depth [66]. Thus, comparing the diffusion coefficients can provide an insight into the ballistic intermixing across the interface. Here, we have calculated the sample material systems' diffusion coefficient, using the Einstein relationship, [67] as a function of irradiation dose. The diffusion coefficient is calculated as  $D = \frac{\langle r_s^2(t) \rangle}{2nt}$ , where  $\langle r_s^2(t) \rangle$  is the MSD of particle determined over time,  $t$ , in a system with  $n$  dimension. Here,  $n = 3$  for our 3D material systems. Our results indicate that the diffusion coefficient increases with increasing radiation dose, Figure 7. The interdiffusion length is  $\sqrt{Dt}$ , which can be found by the experimental fitting of the measured composition parameters across the interface of the solid solution. The usual way to measure the mixing in molecular dynamics simulations is to determine the diffusion coefficient from the MSD [68]. We have calculated the MSD for all the atoms without any bias because the difference in radiation transparency of the elements involved is negligible. The diffusion coefficient data is calculated after the TS period, i.e., ~1ps, of a cascade event to avoid artificially high diffusion coefficients. The calculated radiation-induced diffusion coefficient for different compositions considered here are presented in Figure 7. These values are consistent with the ones reported for Ni and Ni-based alloys, i.e.,  $10^{-9}$ – $10^{-8}$  m<sup>2</sup>/s [69].

Our results revealed that the 800H-Ni multilayer composite structure has the lowest rate of increase of diffusion coefficient as a function of radiation dose compared to the other material systems considered, Figure 7(f). Thus, the (100) 800H-Ni interface's radiation resistance is highest among these systems. It can be explained by the higher iron percentage, 47%, and iron's high migration energy [31] that results in a sluggish diffusion under irradiation. The  $\text{Ni}_{51}\text{Cr}_{30}\text{Fe}_{19}$  has a higher diffusion coefficient, and thus, a lower radiation resistance than  $\text{Ni}_{60}\text{Cr}_{21}\text{Fe}_{19}$  with equal iron content. The low migration energy barrier of Cr atoms results in the enhanced diffusion of alloys with higher Cr concentrations [31].

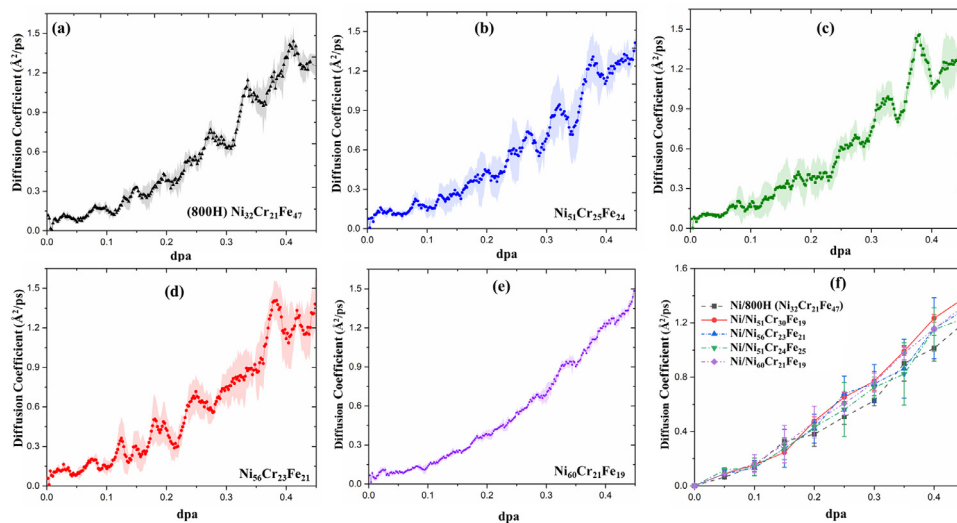


**Figure 7.** Diffusion coefficient as a function of irradiation dose (dpa) in different Ni-Inconel multilayer heterostructure at 1,000K; (a) 800H ( $\text{Ni}_{32}\text{Cr}_{21}\text{Fe}_{47}$ ), (b)  $\text{Ni}_{51}\text{Cr}_{25}\text{Fe}_{24}$ , (c)  $\text{Ni}_{51}\text{Cr}_{30}\text{Fe}_{19}$ , (d)  $\text{Ni}_{56}\text{Cr}_{23}\text{Fe}_{21}$ , and (e)  $\text{Ni}_{60}\text{Cr}_{21}\text{Fe}_{19}$ ; (f) diffusion coefficient of all of them for comparison. Among all these compositions, 800H and  $\text{Ni}_{51}\text{Cr}_{30}\text{Fe}_{19}$  have the lowest and highest rate of increase in the diffusion coefficient, respectively.

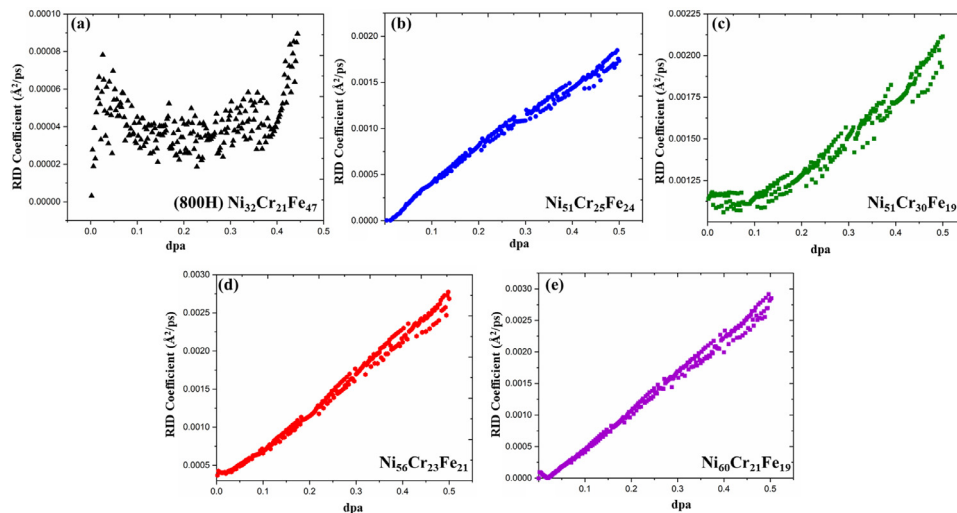


**Figure 8.** Radiation-induced diffusion (RID) coefficient as a function of irradiation dose (dpa) in different Ni-Inconel multilayer heterostructures at 0K; (a) 800H ( $\text{Ni}_{32}\text{Cr}_{21}\text{Fe}_{47}$ ), (b)  $\text{Ni}_{51}\text{Cr}_{25}\text{Fe}_{24}$ , (c)  $\text{Ni}_{51}\text{Cr}_{30}\text{Fe}_{19}$ , (d)  $\text{Ni}_{56}\text{Cr}_{23}\text{Fe}_{21}$ , and (e)  $\text{Ni}_{60}\text{Cr}_{21}\text{Fe}_{19}$ .

The  $\text{Ni}_{56}\text{Cr}_{23}\text{Fe}_{21}$  alloy composition has the third-highest rate of increase of the diffusion coefficient as a function of irradiation dose among all considered compositions. Here, for  $\text{Ni}_{60}\text{Cr}_{21}\text{Fe}_{19}$  Inconel, the Ni content is slightly higher than that for the other compositions. Nevertheless, the percentage of Cr dominates and increases the rate of change of diffusion coefficient by changing the defect dynamics. Cr has a lower migration energy barrier compared to Fe and Ni, which results in its higher diffusivity. The faster diffusion of Cr atoms leads to faster diffusion of vacancies, increasing the probability of having a vacancy next to a Ni atom. Ni's migration energy barrier is very sensitive to vacancies, specifically in their first nearest neighbors. The migration energy of Ni reduces to less than half of its value in the presence of vacancies in its first nearest neighboring sites [57,70]. Thus, due to the higher content of Ni and lower Fe content in the presence of comparable Cr content,  $\text{Ni}_{60}\text{Cr}_{21}\text{Fe}_{19}$  Inconel promotes the formation of Ni-vacancy pairs, specifically during irradiation, as defect concentration increases with radiation dose.

We further performed these irradiation simulations at 0K to understand the role of temperature on radiation-induced mixing of

the two alloys. Figure 8 shows the calculated radiation-induced diffusion coefficient for the considered alloys at 0K. Our results revealed the same linear relationship between the radiation-induced diffusion coefficient and radiation dose, except for the 800H-Ni alloy with almost a constant radiation-induced diffusion coefficient. Therefore, while ballistic intermixing is dominant in Inconel-Ni layered metallic composites, thermal fluctuations play a crucial role in the Incoloy 800H-Ni interface's stability. This can also be explained by the higher iron content of the Incoloy 800H.

During the cascade simulation at 0K, the kinetic energy of the PKA reduced to 0K in ~2fs. Thus, the PKA did not get time to push the atoms out of their Wigner-Seitz cell, and we could not identify any defects.

#### 4. Conclusions

We used molecular dynamics to systematically investigate the radiation-induced mixing at the interface of different metallic alloy compositions of Inconel and pure Ni under the reactor operating conditions. The Inconel-Ni bilayers were subjected to multiple

cascades for a period of 5–6 ns, which corresponded to radiation doses up to 0.5 dpa. We performed a comparative study of damage accumulation for the five material systems. Our results indicate that radiation-induced mixing increases as the radiation damage grows by increasing the radiation dose (dpa). Also, radiation-induced mixing is higher at the initial TS stage of each PKA compared to the relaxed phase, i.e., the ballistic stage.

Investigating the effect of alloy chemistry, we reveal that the 800H has the highest radiation resistance. This resistance is due to its high iron content, 47%, and the fact that the iron has a low diffusivity. Thus, Inconel alloys with high iron content have superiority for defect and radiation damage sensitive applications. Furthermore, increasing Ni content in the Inconel improves the multi-metallic multilayered radiation resistance system involving pure Ni as one of the structural layers. Cr promotes the vacancy and interstitial diffusion and increases the interface thickness, which is due to the low migration energy barrier of Cr atoms. Our results also revealed a linear relationship between the concentration of vacancies and interstitials with the radiation dose. The helium embrittlement of these MMLCs needs to be further investigated, as intergranular fracture has been reported for the Inconel alloys [71]. Our simulations indicate that the (100) interface has a negligible effect on defects' formation and distribution. However, further studies are required to understand the interface orientation's role in forming and distributing defects. We should also note that one of the obstacles to the use of Ni-based alloys as cladding is He buildup under a high concentration of thermal neutrons. Thus, further studies are needed to investigate the effect of He buildup in these alloys for MMLC applications.

## Credit Author Statement

**Shiddartha Paul:** Performed the simulations, analysis, and writing the original draft manuscript; **Daniel Schwen:** Performed the simulations, **Michael Short:** Conceptualization and Methodology, **Kasra Momeni:** Conceptualization, Supervision, Reviewing and Editing.

## Declaration of Competing Interest

The authors declare that they have no known competing financial interests or personal relationships that could have appeared to influence the work reported in this paper.

## Acknowledgment

This project is partly supported by DoE-ARPA-E OPEN (DE-AR0001066), NASA-EPSCoR, the University of Alabama, the Unite National Science Foundation 2D Crystal Consortium – Material Innovation Platform (2DCC-MIP) under NSF cooperative agreement DMR-1539916, and the NSF-CAREER under NSF cooperative agreement CBET-2042683. The authors want to thank Prof. Anna S. Erickson and Dr. Mario Hernandez for their help.

## Supplementary materials

Supplementary material associated with this article can be found, in the online version, at [doi:10.1016/j.jnucmat.2021.152778](https://doi.org/10.1016/j.jnucmat.2021.152778).

## Appendix A. Calculating Radiation Damage using SRIM

We used the following equation to calculate the radiation dose [72]:

$$dpa = Damage \left( \frac{Number}{Angstrom - Ion} \right) \times Fluence \left( \frac{Ion}{Angstrom^2} \right) \times atomic\ volume \left( \frac{Angstrom^3}{atom} \right).$$

The value of damage (number/angstrom-ion) is calculated from the SRIM software package [34]. The fluence (ion/Angstrom<sup>2</sup>) is determined by the reactor problem and indicates the number of incident atoms per unit area. The atomic volume is also calculated as  $\frac{4}{3}\pi r^3$ , where  $r$  is the atomic radius. We have calculated the dpa for a single incident cascade around  $2 \times 10^{-3}$  dpa, which showed a negligible variation in terms of the calculated dpa for alloy systems considered in this study. We have also verified our procedure by reproducing the radiation dose calculated in Ref. [73].

## Appendix B. Forcefield Model

The EAM potential has a general expression:

$$E_{sys} = \frac{1}{2} \sum_{i=1}^N \sum_{j=i_1}^{i_N} \varphi_{ij}(r_{ij}) + \sum_{i,j} F_I(\rho_i). \quad (B-2)$$

Here,  $\varphi_{ij}(r_{ij})$  is the energy between the atoms'  $i$  and  $j$  that is a function of their separation distance,  $r_{ij}$ , and  $F_I(\rho_i)$  is the energy for embedding atom  $i$  into the material with the local atomic density  $\rho_i$ , where

$$\rho_i = \sum_{j=i_1}^{i_N} \rho_j^a(r_{ij}). \quad (B-3)$$

Here,  $\rho_j^a$  is the atomic density contribution from atom  $j$  to the site  $i$  and it can be expressed as

$$\rho_j^a(r) = \rho_{0,I} \exp\left(\frac{r - r_{0,II}}{r_{0,II}}\right) f_{c,II}(r), \quad (B-4)$$

Where,  $\rho_{0,I}$  is the function that captures the decay of electron density with separation distance without affecting the embedding energy. This potential function has been successfully utilized for various alloy material and their responses with the retuned values for each alloying system [74].

$$\varphi_{ij}(r) = \frac{E_{b,II}}{\beta_{ij} - \alpha_{ij}} \left\{ \beta_{ij} \exp\left(-\alpha_{ij} \frac{r - r_{0,II}}{r_{0,II}}\right) - \alpha_{ij} \exp\left(\beta_{ij} \frac{r - r_{0,II}}{r_{0,II}}\right) + \varepsilon_{ij} \exp\left[\lambda_{ij}(r - \delta_{ij})^2\right] \right\} f_{c,II}(r). \quad (B-5)$$

Here,  $E_{b,II}$ ,  $\beta_{ij}$ ,  $\alpha_{ij}$ ,  $r_{0,II}$ ,  $\varepsilon_{ij}$ ,  $\lambda_{ij}$  and  $\delta_{ij}$  are seven  $II$  dependent parameters, and the cutoff function  $f_{c,II}(r)$ ,

$$\varphi_{ij}(r) = \begin{cases} \frac{1}{2} \operatorname{erfc} \left[ \frac{\mu(r - r_{s,II}) + \nu(r_{c,II} - r)}{r_{c,II} - r_{s,II}} \right] & r < r_{c,II} \\ 0, & r \geq r_{c,II} \end{cases}, \quad (B-6)$$

where  $r_{c,II}$  and  $r_{s,II}$  are two independent parameters for the  $II$  pairs (depends on species) and  $\mu$  and  $\nu$  are constants, where  $\frac{1}{2} \operatorname{erfc}(\nu) = 0.9$  and  $\frac{1}{2} \operatorname{erfc}(\mu) = 10^{-5}$ .

In the total energy expression of ZBL modified EAM potential (Eq.B-1), the ZBL term can be expressed as

$$E_{ZBL} = \frac{1}{4\pi\epsilon_0} \frac{Z_i Z_j e^2}{r_{ij}} \varphi(r_{ij}/a) \quad (B-7)$$

Here,  $e$  is the electron charge and  $Z_i$  and  $Z_j$  are the nuclear charges of the two  $i$ 'th and  $j$ 'th atoms,  $a$  is an empirical functional variable

$$a = \frac{0.46850}{Z_i^{0.23} + Z_j^{0.23}}, \quad (B-8)$$

$$H(r_{ij}) = \frac{0.46850}{Z_i^{0.23} + Z_j^{0.23}}, \quad (B-9)$$

$$\varphi = 0.1875e^{-3.19980x} + 0.50986e^{-9.4299x} + 0.28022e^{-0.40290x} + 0.02817e^{-2.0162x}. \quad (B-10)$$

In Eq. (B-10),  $x$  represents the term  $r_{ij}/a$ , and  $r_{ij}$  is the interatomic distance between the atom  $i$  and atom  $j$ .

## References

- [1] S.J. Zinkle, G.S. Was, Materials challenges in nuclear energy, *Acta Mater.* 61 (2013) 735–758, doi:10.1016/j.actamat.2012.11.004.
- [2] S.J. Zinkle, L.L. Snead, Designing Radiation Resistance in Materials for Fusion Energy, *Annu. Rev. Mater. Res.* 44 (2014) 241–267, doi:10.1146/annurev-matsci-070813-113627.
- [3] A.A. Rezwan, M.R. Tonks, M.P. Short, Evaluations of the performance of multi-metallic layered composite cladding for the light water reactor accident-tolerant fuel, *J. Nucl. Mater.* 535 (2020) 152136, doi:10.1016/j.jnucmat.2020.152136.
- [4] M.P. Short, R.G. Ballinger, A Functionally Graded Composite for Service in High-Temperature Lead- and Lead-Bismuth-Cooled Nuclear Reactors—I: Design, *Nucl. Technol.* 177 (2012) 366–381, doi:10.13182/NT12-A13481.
- [5] G. Muralidharan, D.F. Wilson, L.R. Walker, M.L. Santella, D.E. Holcomb, *Cladding Alloys for Fluoride Salt Compatibility*, Oak Ridge Natl. Lab. (2011).
- [6] L. Pathade, T.L. Doane, R.D. Slaton, M.M. Maye, Understanding the Oxidation Behavior of Fe/Ni/Cr and Fe/Cr/Ni Core/Alloy Nanoparticles, *J. Phys. Chem. C* 120 (2016) 22035–22044, doi:10.1021/acs.jpcc.6b06926.
- [7] S. Zhao, Y. Osetsky, A.V. Barashev, Y. Zhang, Acta Materialia Frenkel defect recombination in Ni and Ni – containing concentrated solid – solution alloys, *Acta Mater.* 173 (2019) 184–194, doi:10.1016/j.actamat.2019.04.060.
- [8] M.-H. Tsai, Physical Properties of High Entropy Alloys, *Entropy* 15 (2013) 5338–5345, doi:10.3390/e1512538.
- [9] C.P. Paul, P. Ganesh, S.K. Mishra, P. Bhargava, J.A. Negi, A.K. Nath, Investigating laser rapid manufacturing for Inconel-625 components, *Opt. Laser Technol.* 39 (2007) 800–805.
- [10] T. Trosch, J. Strößner, R. Völkl, U. Glatzel, Microstructure and mechanical properties of selective laser melted Inconel 718 compared to forging and casting, *Mater. Lett.* 164 (2016) 428–431.
- [11] J.J. Holmes, IRRADIATION-INDUCED SWELLING IN NICKEL ALLOYS., 1969.
- [12] A.D. Brailsford, R. Bullough, The rate theory of swelling due to void growth in irradiated metals, *J. Nucl. Mater.* 44 (1972) 121–135.
- [13] N. Ghoniem, G.L. Kulcinski, Swelling of metals during pulsed irradiation, *J. Nucl. Mater.* 69 (1978) 816–820.
- [14] M.A. Khan, S. Sundarrajan, S. Natarajan, P. Parameswaran, E. Mohandas, Oxidation and hot corrosion behavior of nickel-based superalloy for gas turbine applications, *Mater. Manuf. Process.* 29 (2014) 832–839.
- [15] P.R. Okamoto, L.E. Rehn, Radiation-induced segregation in binary and ternary alloys, *J. Nucl. Mater.* 83 (1979) 2–23, doi:10.1016/0022-3115(79)90587-7.
- [16] O. Senninger, F. Soisson, E. Martínez, M. Nastar, C.-C. Fu, Y. Bréchet, Modeling radiation induced segregation in iron–chromium alloys, *Acta Mater.* 103 (2016) 1–11, doi:10.1016/j.actamat.2015.09.058.
- [17] R.A. Holt, Mechanisms of irradiation growth of alpha-zirconium alloys, *J. Nucl. Mater.* 159 (1988) 310–338.
- [18] T. Allen, J. Busby, M. Meyer, D. Petti, Materials challenges for nuclear systems, *Mater. Today* 13 (2010) 14–23.
- [19] W. Han, E.G. Fu, M.J. Demkowicz, Y. Wang, A. Misra, Irradiation damage of single crystal, coarse-grained, and nanograined copper under helium bombardment at 450 C, *J. Mater. Res.* 28 (2013) 2763–2770.
- [20] A. BOLTAX, J.P. FOSTER, R.A. WEINER, A. BIANCHERIA, VOID SWELLING AND IRADIATION CREEP RELATIONSHIPS, in: Meas. Irradiation-Enhanced Creep *Nucl. Mater.*, Elsevier, 1977, pp. 174–183, doi:10.1016/B978-0-7204-0572-9.50023-X.
- [21] C. Lu, K. Jin, L.K. Béland, F. Zhang, T. Yang, L. Qiao, Y. Zhang, H. Bei, H.M. Christen, R.E. Stoller, Direct observation of defect range and evolution in ion-irradiated single crystalline Ni and Ni binary alloys, *Sci. Rep.* 6 (2016) 19994.
- [22] M. Song, M. Wang, X. Lou, R.B. Rebak, G.S. Was, Radiation damage and irradiation-assisted stress corrosion cracking of additively manufactured 316L stainless steels, *J. Nucl. Mater.* 513 (2019) 33–44, doi:10.1016/j.jnucmat.2018.10.044.
- [23] I. Szlufarska, P. Voyles, M. Tonks, Radiation-induced Swelling and Microcracking in SiC Cladding for LWRs, 2019.
- [24] E. Zarkadoula, S.L. Daraszewicz, D.M. Duffy, M.A. Seaton, I.T. Todorov, K. Nordlund, M.T. Dove, K. Trachenko, Electronic effects in high-energy radiation damage in iron, *J. Phys. Condens. Matter.* 26 (2014) 085401, doi:10.1088/0953-8984/26/8/085401.
- [25] S. Li, Q. Wei, Y. Shi, Z. Zhu, D. Zhang, Microstructure Characteristics of Inconel 625 Superalloy Manufactured by Selective Laser Melting, *J. Mater. Sci. Technol.* 31 (2015) 946–952, doi:10.1016/j.jmst.2014.09.020.
- [26] I.K. Suh, H. Ohta, Y. Waseda, High-temperature thermal expansion of six metallic elements measured by dilatation method and X-ray diffraction, *J. Mater. Sci.* 23 (1988) 757–760, doi:10.1007/BF01174717.
- [27] S. Plimpton, P. Crozier, A. Thompson, LAMMPS-large-scale atomic/molecular massively parallel simulator, *Sandia Natl. Lab.* 18 (2007) 43.
- [28] X.W. Zhou, M.E. Foster, R.B. Sills, An Fe-Ni-Cr embedded atom method potential for austenitic and ferritic systems, *J. Comput. Chem.* 39 (2018) 2420–2431.
- [29] G. Bonny, N. Castin, D. Terentyev, Interatomic potential for studying ageing under irradiation in stainless steels: the FeNiCr model alloy, *Model. Simul. Mater. Sci. Eng.* 21 (2013) 85004, doi:10.1088/0965-0393/21/8/085004.
- [30] L.K. Béland, A. Tamm, S. Mu, G.D. Samolyuk, Y.N. Osetsky, A. Aabloo, M. Klinenberg, A. Caro, R.E. Stoller, Accurate classical short-range forces for the study of collision cascades in Fe-Ni-Cr, *Comput. Phys. Commun.* 219 (2017) 11–19, doi:10.1016/j.cpc.2017.05.001.
- [31] D. Chakraborty, D.S. Aidhy, Cr-induced fast vacancy cluster formation and high Ni diffusion in concentrated Ni-Fe-Cr alloys, *J. Alloys Compd.* 725 (2017) 449–460, doi:10.1016/j.jallcom.2017.07.140.
- [32] M.W. Ullah, D.S. Aidhy, Y. Zhang, W.J. Weber, Damage accumulation in ion-irradiated Ni-based concentrated solid-solution alloys, *Acta Mater.* 109 (2016) 17–22, doi:10.1016/j.actamat.2016.02.048.
- [33] M.W. Ullah, Y. Zhang, N. Sellami, A. Debelle, H. Bei, W.J. Weber, Evolution of irradiation-induced strain in an equiatomic NiFe alloy, *Scr. Mater.* 140 (2017) 35–39, doi:10.1016/j.scriptamat.2017.06.042.
- [34] J.F. Ziegler, M.D. Ziegler, J.P. Biersack, SRIM – The stopping and range of ions in matter (2010), *Nucl. Instruments Methods Phys. Res. Sect. B Beam Interact. with Mater. Atoms.* 268 (2010) 1818–1823, doi:10.1016/j.nimb.2010.02.091.
- [35] J.F. Ziegler, J.P. Biersack, *The stopping and range of ions in matter*, in: *Treatise Heavy-Ion Sci.*, Springer, 1985, pp. 93–129.
- [36] E. del Rio, J.M. Sampedro, H. Dogo, M.J. Caturla, M. Caro, A. Caro, J.M. Perlado, Formation energy of vacancies in FeCr alloys: Dependence on Cr concentration, *J. Nucl. Mater.* 408 (2011) 18–24, doi:10.1016/j.jnucmat.2010.10.021.
- [37] S.M. Kim, W.J.L. Buyers, Vacancy formation energy in iron by positron annihilation, *J. Phys. F Met. Phys.* 8 (1978) L103–L108, doi:10.1088/0305-4608/8/5/001.
- [38] W. Wycisk, M. Feller-Kniepmeier, Quenching experiments on high-purity nickel, *Phys. Status Solidi* 37 (1976) 183–191, doi:10.1002/pssa.2210370124.
- [39] G. Martin, C. Sabathier, J. Wiktor, S. Maillard, Molecular dynamics study of the bulk temperature effect on primary radiation damage in uranium dioxide, *Nucl. Instruments Methods Phys. Res. Sect. B Beam Interact. with Mater. Atoms.* 352 (2015) 135–139.
- [40] F. Seitz, On the theory of diffusion in metals, *Acta Crystallogr* 3 (1950) 355–363, doi:10.1107/S0365110X0000999.
- [41] N.-Y. Park, Y.-C. Kim, H.-K. Seok, S.-H. Han, S. Cho, P.-R. Cha, Molecular dynamics simulation of irradiation damage in tungsten, *Nucl. Instruments Methods Phys. Res. Sect. B Beam Interact. with Mater. Atoms.* 265 (2007) 547–552, doi:10.1016/j.nimb.2007.10.003.
- [42] L. Zhang, M.J. Demkowicz, Radiation-induced mixing between metals of low solid solubility, *Acta Mater.* 76 (2014) 135–150.
- [43] Y. Zhang, K. Jin, H. Xue, C. Lu, R.J. Olsen, L.K. Béland, M.W. Ullah, S. Zhao, H. Bei, D.S. Aidhy, G.D. Samolyuk, L. Wang, M. Caro, A. Caro, G.M. Stocks, B.C. Larsson, I.M. Robertson, A.A. Correa, W.J. Weber, Influence of chemical disorder on energy dissipation and defect evolution in advanced alloys, *J. Mater. Res.* 31 (2016) 2363–2375, doi:10.1557/jmr.2016.269.
- [44] M. Jin, P. Cao, S. Yip, M.P. Short, Radiation damage reduction by grain-boundary biased defect migration in nanocrystalline Cu, *Acta Mater.* 155 (2018) 410–417, doi:10.1016/j.actamat.2018.05.071.
- [45] P.J. Doyle, K.M. Benensky, S.J. Zinkle, Modeling the impact of radiation-enhanced diffusion on implanted ion profiles, *J. Nucl. Mater.* 509 (2018) 168–180, doi:10.1016/j.jnucmat.2018.06.042.
- [46] M. Jin, P. Cao, M.P. Short, Thermodynamic mixing energy and heterogeneous diffusion uncover the mechanisms of radiation damage reduction in single-phase Ni-Fe alloys, *Acta Mater.* 147 (2018) 16–23.
- [47] M. Range, C. Temperature, INCONEL alloy 718, (n.d.).
- [48] G.S. Was, *Fundamentals of radiation materials science: metals and alloys*, Springer, 2016.
- [49] K. Nordlund, M. Ghaly, R.S. Averback, M. Caturla, T. Diaz de la Rubia, J. Tarus, Defect production in collision cascades in elemental semiconductors and fcc metals, *Phys. Rev. B* 57 (1998) 7556–7570, doi:10.1103/PhysRevB.57.7556.
- [50] E. Zarkadoula, D.M. Duffy, K. Nordlund, M.A. Seaton, I.T. Todorov, W.J. Weber, K. Trachenko, Electronic effects in high-energy radiation damage in tungsten, *J. Phys. Condens. Matter.* 27 (2015) 135401.
- [51] E. Zarkadoula, G. Samolyuk, Y. Zhang, W.J. Weber, Electronic stopping in molecular dynamics simulations of cascades in 3C-SiC, *J. Nucl. Mater.* 540 (2020) 152371, doi:10.1016/j.jnucmat.2020.152371.
- [52] E. Zarkadoula, G. Samolyuk, H. Xue, H. Bei, W.J. Weber, Effects of two-temperature model on cascade evolution in Ni and NiFe, *Scr. Mater.* 124 (2016) 6–10, doi:10.1016/j.scriptamat.2016.06.028.
- [53] E. Zarkadoula, G. Samolyuk, W.J. Weber, Two-temperature model in molecular dynamics simulations of cascades in Ni-based alloys, *J. Alloys Compd.* (2017), doi:10.1016/j.jallcom.2016.12.441.
- [54] N.T.H. Trung, H.S.M. Phuong, M.D. Starostenkov, V.V. Romanenko, V.A. Popov, Threshold displacement energy in Ni, Al and B2 NiAl, *IOP Conf. Ser. Mater. Sci. Eng.* 447 (2018) 012004, doi:10.1088/1757-899X/447/1/012004.

[55] L. Zhang, M.J. Demkowicz, Radiation-induced mixing between metals of low solid solubility, *Acta Mater.* 76 (2014) 135–150, doi:10.1016/j.actamat.2014.05.013.

[56] G.H. Kinchin, R.S. Pease, The Displacement of Atoms in Solids by Radiation, *Reports Prog. Phys.* 18 (1955) 301, doi:10.1088/0034-4885/18/1/301.

[57] S. Choudhury, L. Barnard, J.D. Tucker, T.R. Allen, B.D. Wirth, M. Asta, D. Morgan, Ab-initio based modeling of diffusion in dilute bcc Fe–Ni and Fe–Cr alloys and implications for radiation induced segregation, *J. Nucl. Mater.* 411 (2011) 1–14.

[58] P. Süle, Anomalous atomic transport in driven systems: Ion-sputtering induced enhanced intermixing and cratering in Pt/Ti, *Nucl. Instruments Methods Phys. Res. Sect. B Beam Interact. with Mater. Atoms.* 268 (2010) 1404–1411.

[59] R.S. Averback, T.D. de la Rubia, Displacement Damage in Irradiated Metals and Semiconductors BT – Solid State Physics - Advances in Research and Applications, in: *Solid State Phys. - Adv. Res. Appl.*, Elsevier, 1998, pp. 281–402.

[60] K. Nordlund, J. Tarus, J. Keinonen, M. Ghaly, R.S. Averback, Heat spike effects on ion beam mixing, *Nucl. Instruments Methods Phys. Res. Sect. B Beam Interact. with Mater. Atoms.* 164–165 (2000) 441–452.

[61] C. Lu, L. Niu, N. Chen, K. Jin, T. Yang, P. Xiu, Y. Zhang, F. Gao, H. Bei, S. Shi, Enhancing radiation tolerance by controlling defect mobility and migration pathways in multicomponent single-phase alloys, *Nat. Commun.* 7 (2016) 13564.

[62] P.F. Zou, R.F.W. Bader, A topological definition of a Wigner–Seitz cell and the atomic scattering factor, *Acta Crystallogr. Sect. A Found. Crystallogr.* 50 (1994) 714–725.

[63] K. Jin, W. Guo, C. Lu, M.W. Ullah, Y. Zhang, W.J. Weber, L. Wang, J.D. Poplawsky, H. Bei, Effects of Fe concentration on the ion-irradiation induced defect evolution and hardening in Ni–Fe solid solution alloys, *Acta Mater.* (2016), doi:10.1016/j.actamat.2016.09.025.

[64] W.Z. Han, M.J. Demkowicz, E.G. Fu, Y.Q. Wang, A. Misra, Effect of grain boundary character on sink efficiency, *Acta Mater.* 60 (2012) 6341–6351, doi:10.1016/j.actamat.2012.08.009.

[65] B.N. Singh, A.J.E. Foreman, Calculated grain size-dependent vacancy supersaturation and its effect on void formation, *Philos. Mag.* 29 (1974) 847–858, doi:10.1080/14786437408222075.

[66] R.S. Averback, D. Peak, L.J. Thompson, Ion-beam mixing in pure and in immiscible copper bilayer systems, *Appl. Phys. A.* 39 (1986) 59–64.

[67] J.A. Given, B.B. Mandelbrot, Diffusion on fractal lattices and the fractal Einstein relation, *J. Phys. A. Math. Gen.* 16 (1983) L565–L569, doi:10.1088/0305-4470/16/15/003.

[68] R.S. Averback, T.D. de la Rubia, Displacement Damage in Irradiated Metals and Semiconductors, in: *Solid State Phys. - Adv. Res. Appl.*, Elsevier, 1998, pp. 281–402.

[69] S. Zhao, Y. Osetsky, Y. Zhang, Preferential diffusion in concentrated solid solution alloys: NiFe, NiCo and NiCoCr, *Acta Mater.* 128 (2017) 391–399, doi:10.1016/j.actamat.2017.01.056.

[70] L. Barnard, D. Morgan, Ab initio molecular dynamics simulation of interstitial diffusion in Ni–Cr alloys and implications for radiation induced segregation, *J. Nucl. Mater.* 449 (2014) 225–233, doi:10.1016/j.jnucmat.2013.10.022.

[71] C.D. Judge, N. Gauquelin, L. Walters, M. Wright, J.I. Cole, J. Madden, G.A. Botton, M. Griffiths, Intergranular fracture in irradiated Inconel X-750 containing very high concentrations of helium and hydrogen, *J. Nucl. Mater.* 457 (2015) 165–172, doi:10.1016/j.jnucmat.2014.10.008.

[72] M. Short, Radiation Stopping Power, Damage Cascades, Displacement and the DPA, Massachusetts Inst. Technol. MIT OpenCourseWare. (2015) 1–112.

[73] J. Wang, M.B. Toloczko, N. Bailey, F.A. Garner, J. Gigax, L. Shao, Modification of SRIM-calculated dose and injected ion profiles due to sputtering, injected ion buildup and void swelling, *Nucl. Instruments Methods Phys. Res. Sect. B Beam Interact. with Mater. Atoms.* 387 (2016) 20–28, doi:10.1016/j.nimb.2016.09.015.

[74] X.W. Zhou, J.A. Zimmerman, B.M. Wong, J.J. Hoyt, An embedded-atom method interatomic potential for Pd–H alloys, *J. Mater. Res.* 23 (2008) 704–718, doi:10.1557/JMR.2008.0090.